Laboratory Hydraulic Fracturing of Granite: Acoustic Emission Observations and Interpretation

B. Q. Li[1], B. M. Gonçalves da Silva[2], H. H. Einstein[1]

[1]Department of Civil and Environmental Engineering, Massachusetts Institute of Technology, Cambridge, Massachusetts, USA

[2]Department of Civil and Environmental Engineering, New Jersey Institute of Technology, Newark, New Jersey, USA

Corresponding author: Bing Qiuyi Li (bingqli@mit.edu)

Key Points:

- Acquisition, analysis and interpretation of acoustic emissions from a series of hydraulic fracture experiments on granite with pre-cut flaws
- Hypocenter locations tend to agree well with white patching (process zone) and crack patterns
- Spatio-temporal analysis of focal mechanisms indicate points where microcrack coalescence were detected by AE

Abstract

Hydraulic fracturing is routinely used, but the fracturing processes that occur when rocks are hydraulically-fractured are not entirely understood and require further investigation. This study presents the acquisition, analysis and interpretation of acoustic emissions data from a series of laboratory hydraulic fracturing experiments on granite. Specimens with different orientations of two pre-cut flaws were tested under both 0 MPa and 5 MPa of vertical uniaxial stress to understand the effect of the external stress conditions. Acoustic emissions (AE) data are related to corresponding qualitative visual observations made using high-resolution and high-speed imaging. We find that in general, (1) the AE begin to occur at approximately 80% of peak pressure, (2) the focal mechanisms suggest that 55-60% of the radiation pattern could be explained by a double couple mechanism, (3) hypocenter locations tended to agree well with visually observed white patching (process zone) and crack patterns, (4) spatio-temporal analysis revealed points in time at which microcrack coalescence were detected by AE, and lastly (5) that the AE could be used to make a non-unique prediction of crack initiation.

1 Introduction

Hydraulic fracturing is routinely used, but the fracturing processes that occur when rocks are hydraulically fractured are often not entirely understood and require further investigation.
Many authors have studied the fracturing and hydraulic fracturing of rocks and rock-like materials in the laboratory. Some of them used acoustic emissions (AE) to better understand the mechanisms involved in the initiation and propagation of cracks in rocks. The information that can be obtained from the interpretation of the AE signals includes the number and rate of AE events, which can be related to stages of development of fractures [Li et al., 2015; Bunger et al., 2014; Moradian et al., 2010 and 2016], the location of the events [Savic & Cockram, 1993; Frash, 2014; Ishida, 2001; Mayr et al., 2011; Stanchits et al., 2009, and 2011; Dresen, 2010] and, finally, the source mechanism of the micro-cracks i.e. if they are mainly tensile, shear, or mixed-mode tensile/shear [Graham et al., 2010; Ohtsu, 1995; Matsunaga et al., 1993; Stoeckhert et al., 2015].
This paper draws from the same dataset as presented in Goncalves da Silva and Einstein (2018), where the focus was on the visual observations and their interpretation, while here we discuss the AE monitoring and interpretation. In the tests conducted, prismatic granite specimens were subjected to two different constant vertical stresses (0 and 5 MPa) while hydraulic pressure was increased inside pre-fabricated fractures (so-called “flaws”) until cracks initiated and propagated. The objective of this paper is to relate the AE produced during the hydraulic fracturing tests to the fracturing processes observed visually (Goncalves da Silva and Einstein, 2018). In order to achieve this objective, the amplitudes, rates, hypocenter locations and focal mechanisms of the AE were analyzed and interpreted at successive stages of crack development.
Section 2 describes the measurement methodology, including the installation of the AE sensors, and the AE data analyzed. Section 3 presents the results of the experiments, discussing rate and amplitude of AE, focal mechanisms, and the hypocenter locations. Finally, section 4 presents the conclusions.

2 Methodology

2.1 Physical Setup

The experimental setup is described in detail in other publications (Goncalves da Silva et al., 2015; Goncalves da Silva and Einstein 2018) and is summarised here. Specimens of Barre Granite are first cut to dimensions of 1" x 3" x 6", then the flaws are cut with a waterjet to geometries described in Figure 1.

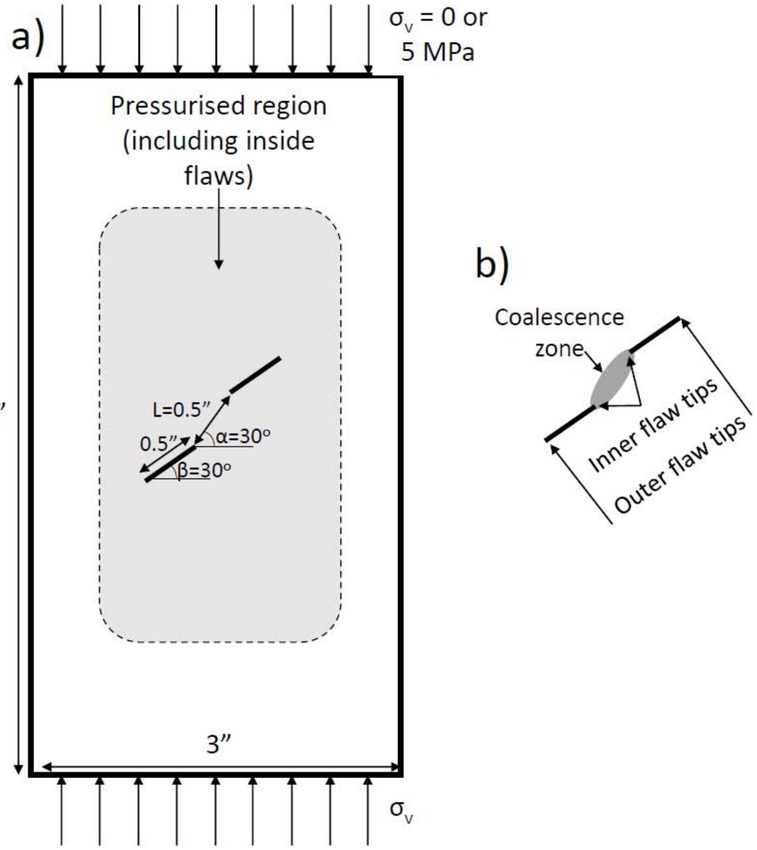

Figure 1: a) Schematic of the specimen setup including L-β-α naming convention and boundary conditions for tests used in this paper. VL0 refers to experiments with 0 MPa of applied vertical stress, VL5 with 5 MPa of vertical stress. For example, the specimen above is 2a-30-30-VL5, indicating a 30 degree inclination of the flaws (β) and 30 degrees between the flaws (bridging angle α), and 5 MPa of vertical stress. b) Notation denoting regions surrounding the pre-cut flaws.

The specimen is clamped inside the hydraulic fracturing device (Figure 2), which applies water pressure to the face of the specimen as well as inside the flaws (Figure 1 and 2), and is placed in the Baldwin load frame (Figure 3). A constant vertical stress of 0 or 5 MPa is then applied, and the specimen is finally loaded to failure using water pressure, which is increased in 0.5 MPa increments. The measurements in these tests are: AE, time-pressure data, high resolution images throughout the test, and high speed (14 000 fps) video taken in a 2-second window around fracture initiation.

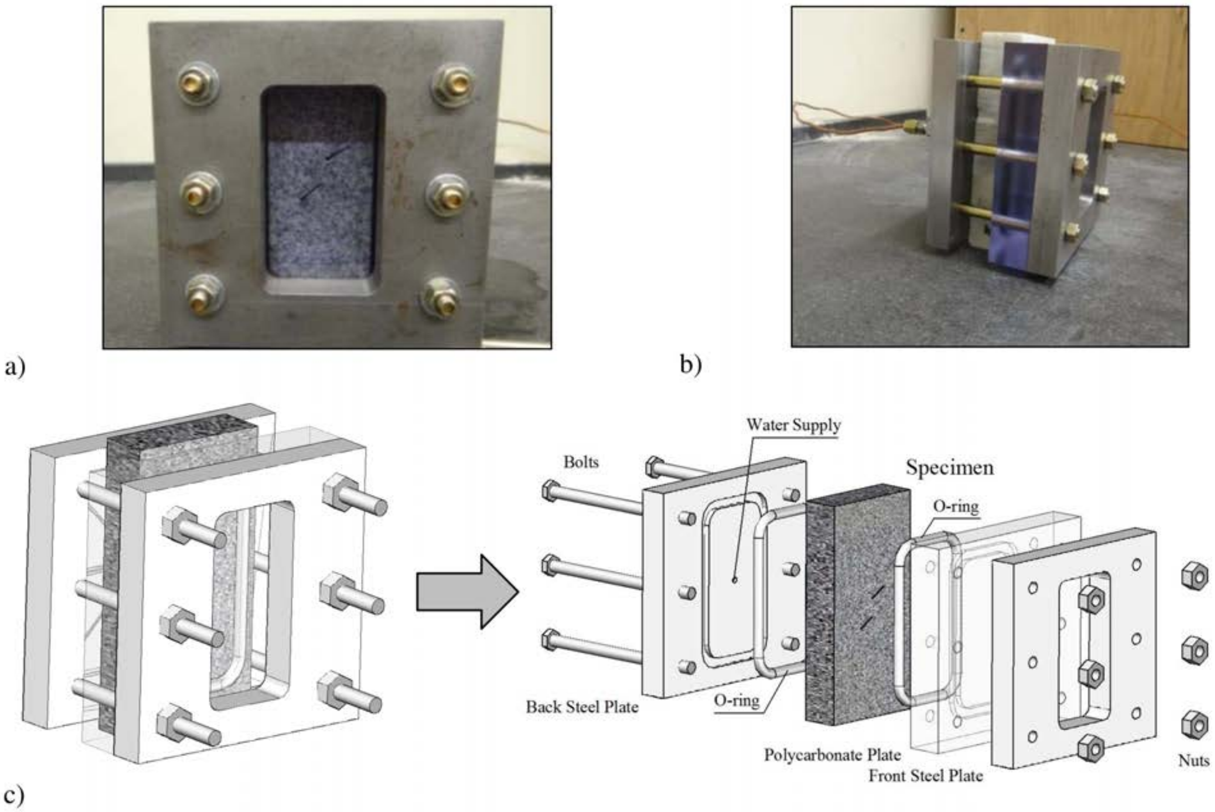

Figure 2: a) Front and b) oblique view of the pressurisation device used in hydraulic fracturing tests; c) schematic showing the different parts of the device. (From Goncalves da Silva et al, 2015)

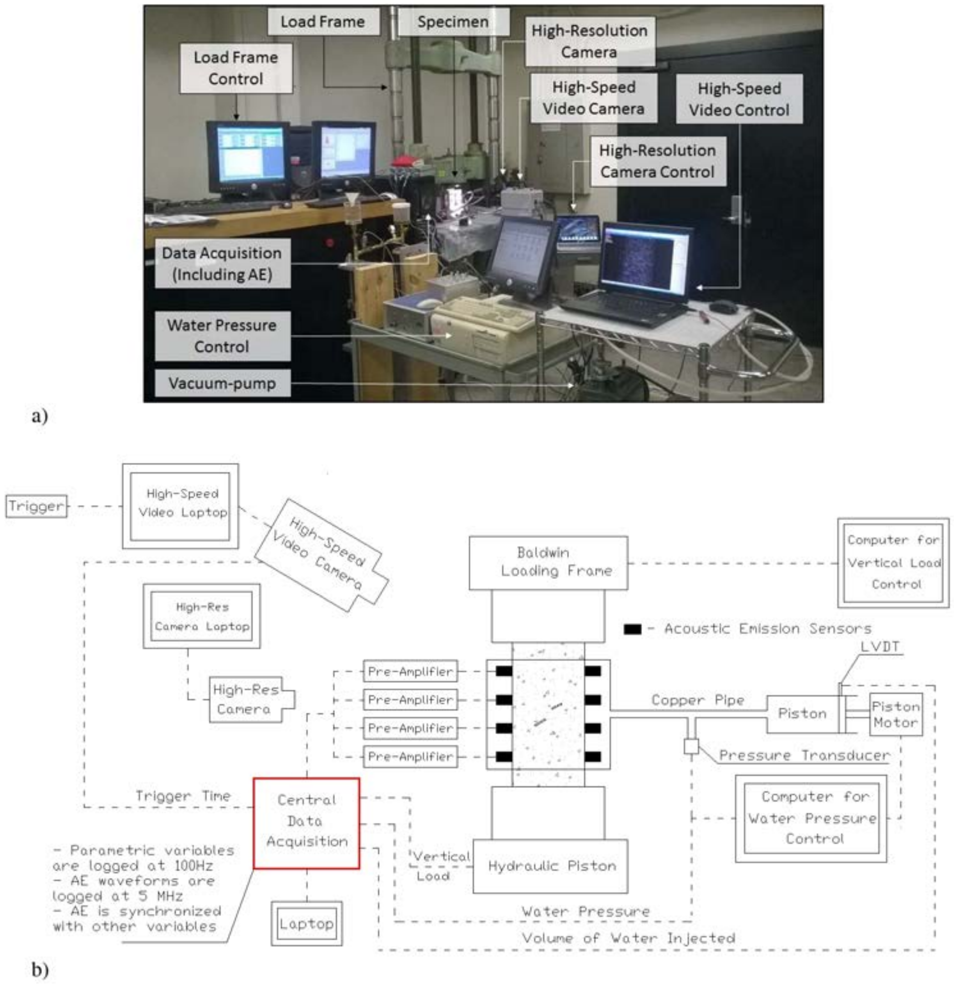

Figure 3: a) Overall view and b) schematic of the test setup used in the hydraulic fracturing tests. (After Goncalves da Silva et al. 2015)

2.2 AE Setup

The experiments are instrumented with eight PAC (Physical Acoustics Corporation) Micro30S sensors, attached with 0.002" acrylic double-sided tape and fixed in place with hot-glue, as shown in Figure 4. All sensors were connected to PCI-2 data acquisition cards from PAC at a sampling rate of 5 MHz using an amplification of 20 dB; a 35 dB threshold was used, i.e. the system recorded waveforms upon registering any amplitude greater than 35 dB. Given that the specimens tended to produce a significant amount of emissions for a period of a few seconds immediately prior to and during the rock fracturing process, it was necessary to modify the system for continuous recording to maximise signal recording during fracturing. These efforts resulted in a system that recorded 84% of all data when the system was detecting a continuous signal longer than a few seconds (Li et al., 2015).

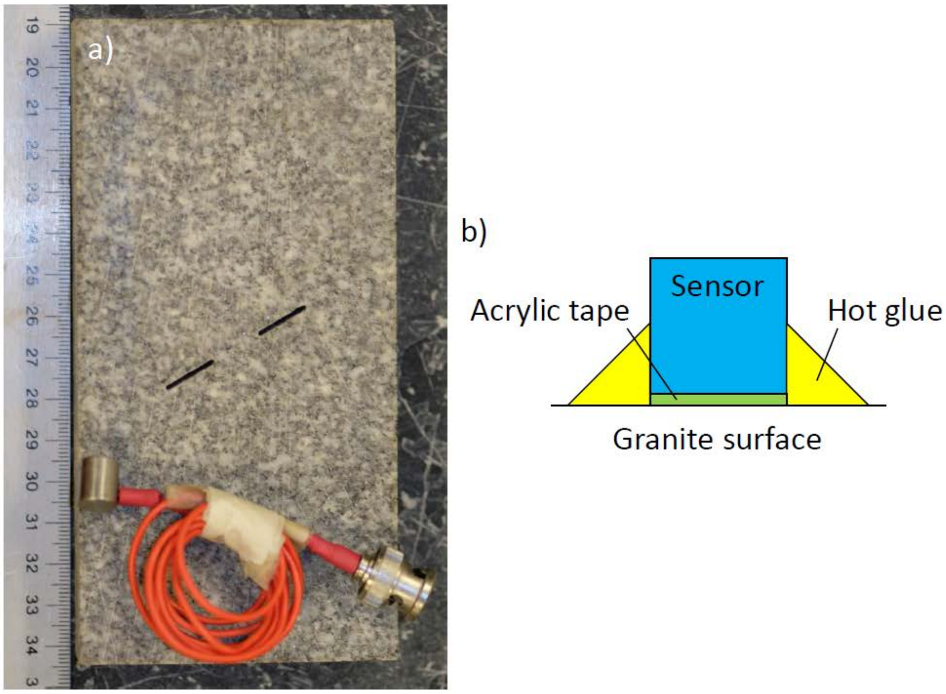

Figure 4: a) Acoustic emission sensors used in the hydraulic fracturing tests b) Side view of the attachment between the sensor and the specimen using double-sided tape and hot-glue

Due to the high rate of AE activity, it was necessary to develop an arrival picking algorithm capable of selecting from a rapid series of events, as seen in Figure 5. The picker consists of dividing any recording into segments shorter than the expected time between events. The Akaike information criterion (AIC) value (Maeda, 1985) was then calculated for each segment, and peaks greater than an empirically determined AIC value were taken to be arrivals. However, this can result in false detections from the signal tail, as seen at 2056.4422s and 2056.4437s (Red circles) in Figure 5c. To resolve this issue, the algorithm only takes the arrivals where the signal amplitude as measured by the root mean squared is larger after the arrival than before. We empirically determined that a time segment of 0.4 ms and minimum AIC peak of 3 x10-5 s·log(V2) to be appropriate parameters for the tested material and loading conditions.

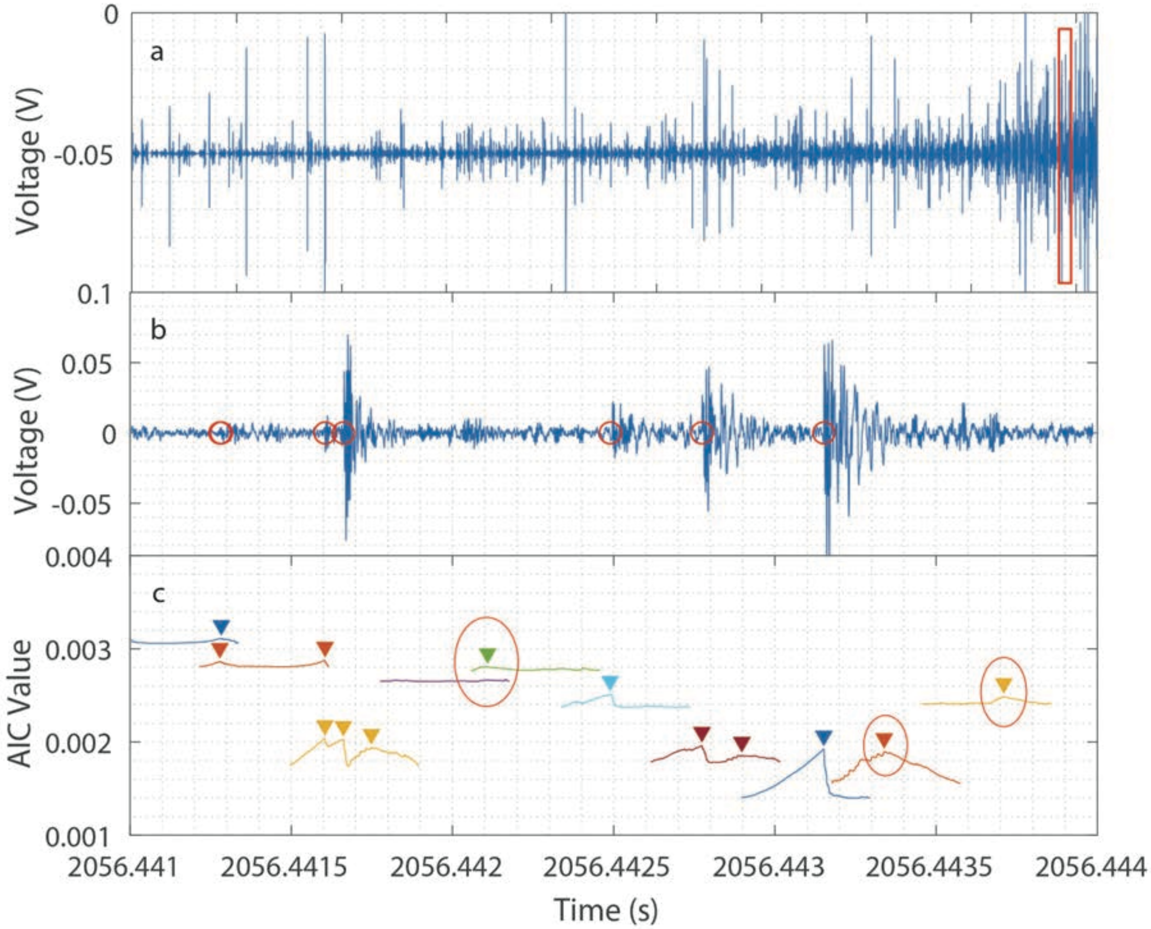

Figure 5: a) Waveform data over 0.46 s period immediately prior to failure. b) Close-up of red box in subfigure a, with automatic picks shown in red circles. c) Segmented AIC values for the waveform data shown in subfigure b. Notable peaks in AIC value shown with triangles, while red circles denote false detections.

Locations were determined from the minimisation of residuals as outlined in Shearer (2009) using a constant velocity model of 4600 m/s, as measured on the specimen under load and water pressure during the test. We optimised with the fminsearch function in MATLAB using an error tolerance of 1 mm on all arrivals and a minimum requirement of 4 arrival detections (Figure 6). Any microseismic disturbance that can be localised is considered an “event” in this study. Focal mechanisms were determined from moment tensor inversion on events with five or more P-wave arrival detections according to the 2D implementation of the SiGMA (Ohtsu, 2000) algorithm where we assume that $M13 = M23 = 0$ and $M33 = \nu\cdot(M11+M22)$. Decomposition was done using the ratios of the eigenvalues of the moment tensor to obtain the double couple (DC), compensated linear vector dipole (CLVD) and isotropic (ISO) proportions for each event according to Vavryčuk (2015). This convention defines +CLVD, - CLVD, +ISO and –ISO as tensile cracks, anti-cracks, explosions, and implosions respectively (Figure 7). Events with a double couple (DC) component greater than 50% are considered shear, and non double couple (NDC) otherwise. The NDC events are separated into explosive and implosive events, based on whether the ISO and CLVD ratios are positive or negative, respectively, as illustrated in Figure

7. Note that in this decomposition scheme the ISO and CLVD proportions always share the same sign, but that there are many alternative interpretations and decompositions of the moment tensor (Julian and Sipkin, 1985). The AE setups for each individual experiment were not calibrated for absolute magnitudes, and so the amplitudes presented in this study are only relative within an individual experiment. In general, based on other studies with this system (Li and Einstein, 2017) and similar laboratory-scale rock setups (McLaskey et. al, 2015; Yoshimitsu et al, 2014), the magnitudes should range between approximately Mw = -5 to -8.

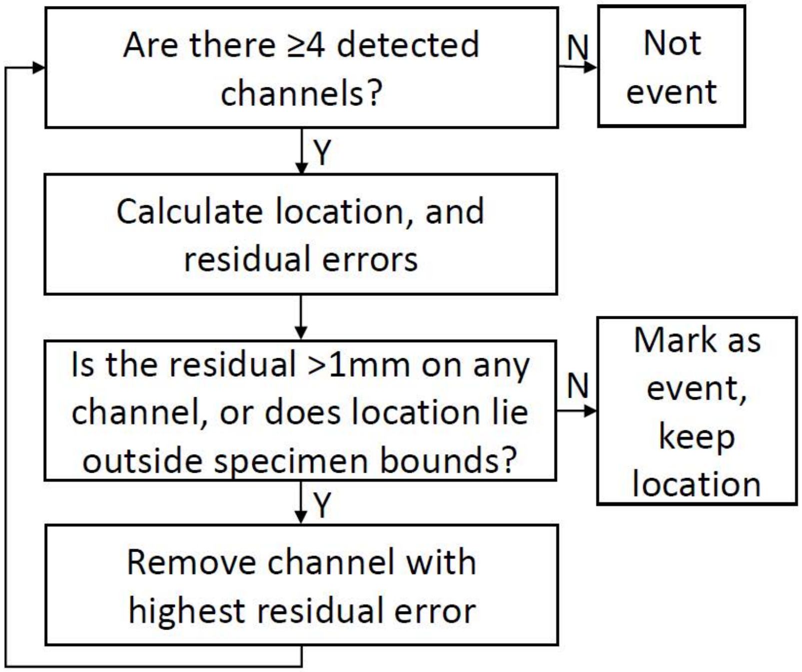

Figure 6: Algorithm used to calculate hypocenter locations for AE events

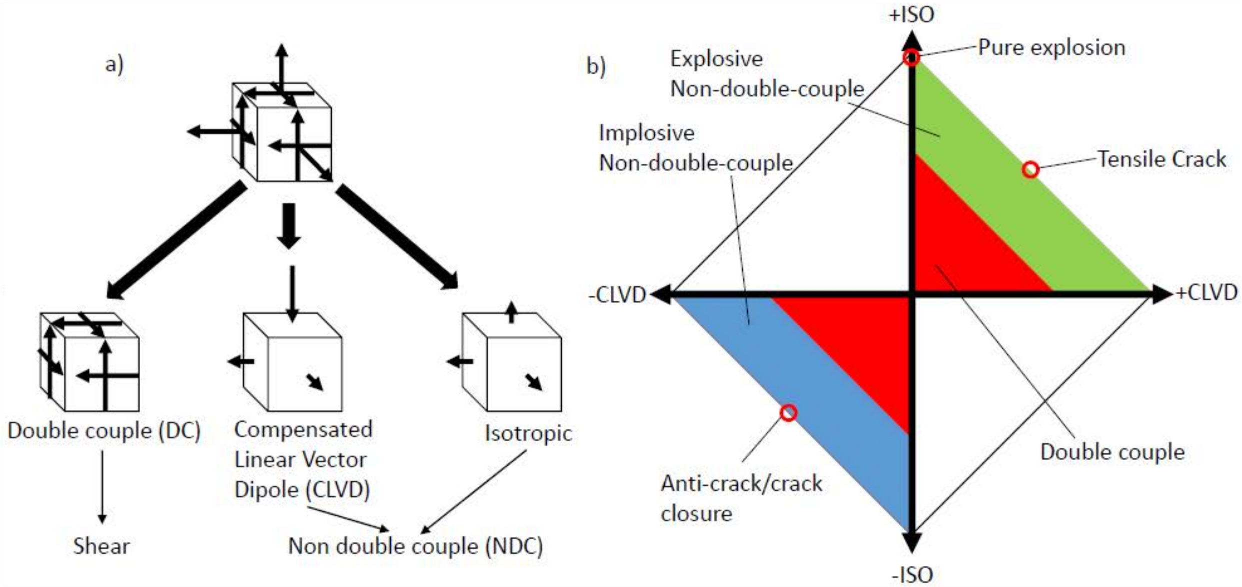

Figure 7: a) Illustration of moment tensor decomposition. Adapted from Grosse and Ohtsu (2008). b) Diamond CLVD-ISO plot illustrating AE event classification used in this study. After Vavryčuk (2015).

3 Results

3.1 Rate of AE events over time

Figure 8 shows the pressure-time data and the rate of AE hits (individual detections on any channel) for the 13 tests presented in this study, along with the time at which white patching is first observed. Recall (Figure 1) that "white patching" refers to zones consisting of microcracks (process zone), which are detected visually by a change in the refractive properties of the rock (Wong and Einstein, 2009).

In general, AE associated with development of the hydraulic fracture begin at the start of the last or second last pressure stages, at which point the AE rate increases exponentially (linearly in log space). This corresponds to approximately 80% of maximum water pressure, which is relatively close to the peak driving load; this is in contrast to rock specimens brought to failure in compression (Yoshimitsu et al., 2014; Chang and Lee, 2004; Moradian et. al. 2016), where the AE begin to consistently occur at 25-50% of peak load.

In some experiments, such as the 2a-30-0-VL0-C, 2a-30-120-VL5-B, and both single flaw geometries, the rate reaches another inflection whereupon the rate increases again (denoted as secondary rate in the Figure 8); suggesting the onset of another mechanism. This tended to occur around 90% of peak pressure. We also observe that the AE rate tends to increase on the pressure stage immediately following first detection of white patching, suggesting that the white patching is well correlated to the onset of microseismic activity.

Since the pressure was increased in 0.5 MPa steps, the rate of pressure application was not constant, and so fracturing occurred in some tests during an increase in pressure (e.g. 2a-30-30-VL5-C), while in other tests during a period of constant pressure (e.g. 2a-30-30-VL0-C). However, this does not appear to have a significant effect on this experimental series, since for all tests the AE hit rate appears to exhibit similar behaviour regardless of whether the pressure was static or increasing leading up to fracturing (Note on Figure 8 as constant or rising pressure respectively). Specifically, in each test the hit rate increases over approximately 5-10 seconds up to the time at which the pressure drops, which corresponds to fracture initiation (Li et al., 2015). However, the fact that we, in some cases, observe a hydraulic fracture developing at a constant water pressure indicates that there may be time dependent effects (Liu et al., 2001).

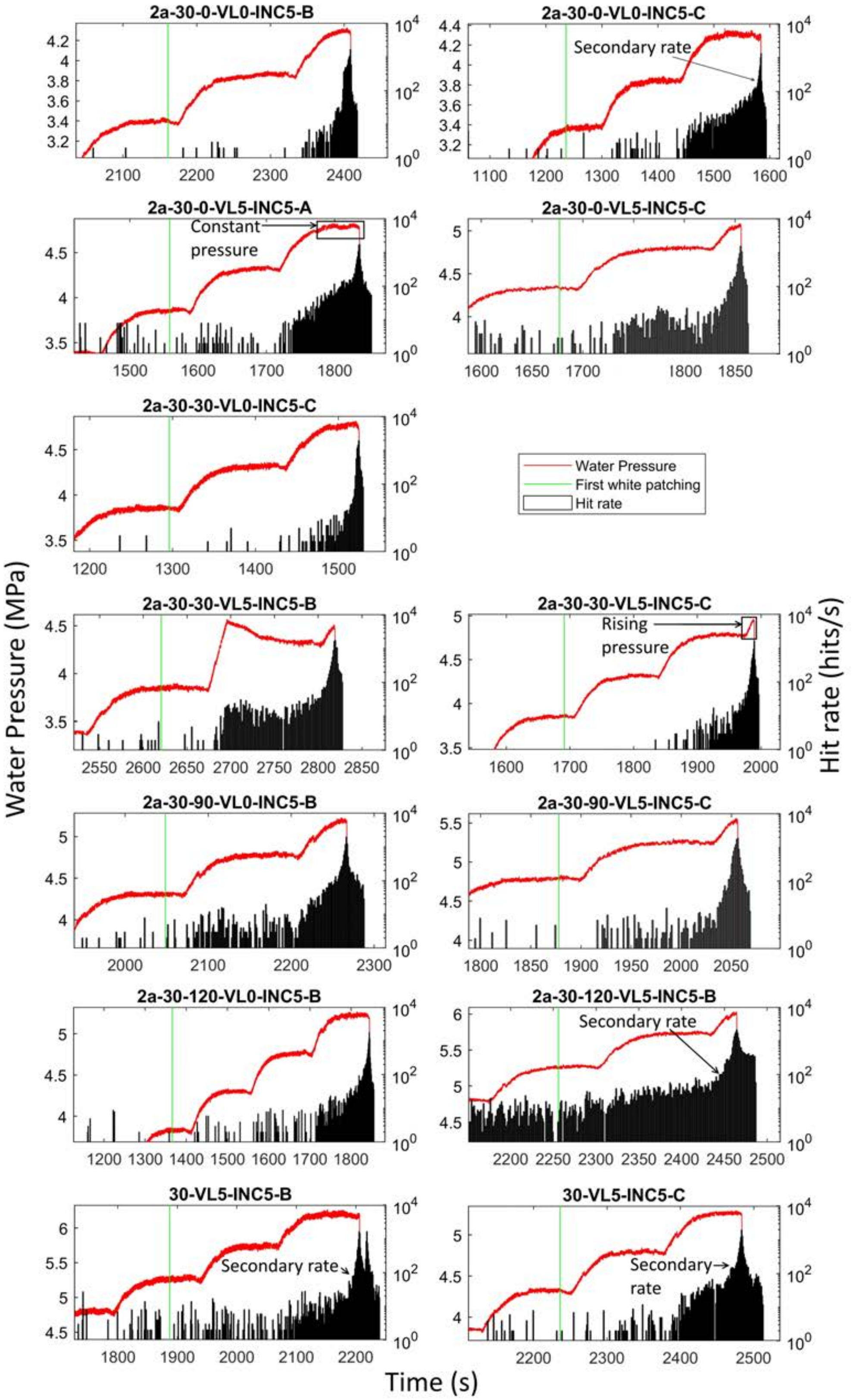

Figure 8: Water pressure, time of first white patching and rate of AE hits for each test. Arrows and black boxes indicate phenomena commented on in the text.

3.2 Amplitude of AE over time

Figure 9 shows the amplitude of AE hits that occur towards the end of each experiment. One can see that in most cases, peak amplitudes occur immediately before the drop in water pressure corresponding to the fracture initiation and propagation. We can also see that, in general, the average amplitude fluctuates significantly in the seconds immediately prior to fracture, as individual microseismic events reflect microcracks that can be seen in the white patching discussed in the following sections. In general, the hit amplitude tends to follow a similar trend to the rate of AE hits shown in Figure 8, in that the average hit amplitude tends to increase along with the hit rate. There does not appear to be a significant relation between the amplitude and the time at which white patching is first detected.

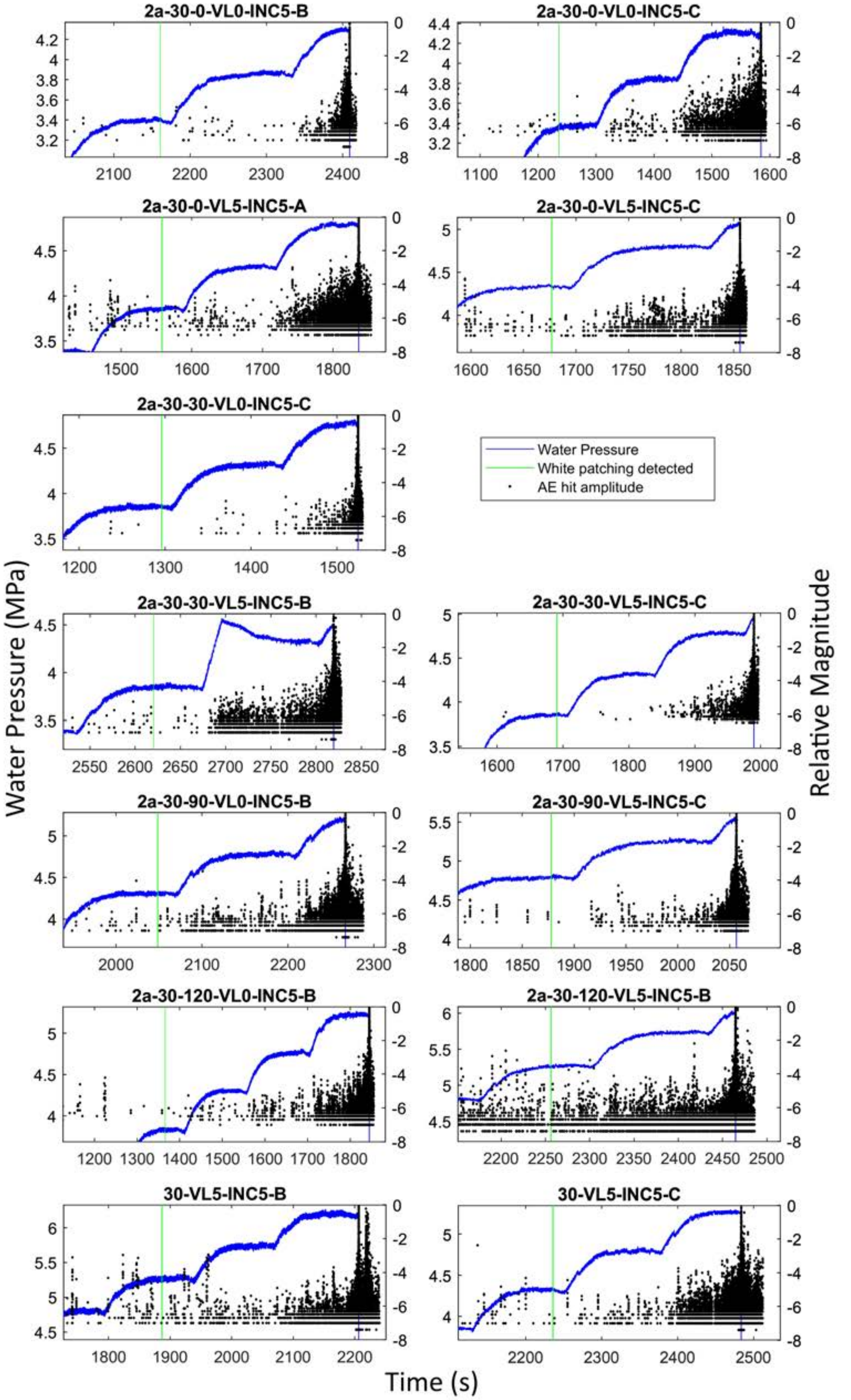

Figure 9: Water pressure (blue line) and AE amplitude (scatter data) over time. Green line the time at which white patching was first detected visually.

3.3 Focal Mechanisms

General AE characteristics are listed in Table 1. The number of events generally increases with increasing bridging angle, and tests with a single flaw produced a larger number of events compared to the 2a-30-0 and 2a-30-30 geometries. Overall, the tests with the most events correspond to those with higher breakdown pressure, which intuitively makes sense given that higher pressure supplies a larger amount of energy to the system. However, there does not appear to be a significant difference between the number of events produced by tests confined by a vertical stress of 5 MPa as opposed to those at 0 MPa.

Table 1: Summary of test data from the hydraulic fracture stimulation stage of the experimental series. The focal mechanisms are the cumulative proportion over the hydraulic fracture stage of each experiment. Note that the absolute value of all the focal mechanism proportions sum to 100%, but – CLVD and –ISO are expressed as negative proportions in this study.

Specimen Name	Max Pressure (MPa)	Number of Events	DC (%)	+CLVD (%)	-CLVD (%)	+ISO (%)	-ISO (%)
2a-30-0-VL0-INC5-B	4.3	269	60.5	5.4	-3.7	18.3	-12.0
2a-30-0-VL0-INC5-C	4.3	247	59.4	6.9	-2.5	23.0	-8.2
2a-30-0-VL5-INC5-A	4.8	489	58.7	6.9	-2.6	23.1	-8.7
2a-30-0-VL5-INC5-C	5.1	281	60.5	6.0	-3.1	20.2	-10.2
2a-30-30-VL0-INC5-C	4.8	311	58.0	7.7	-1.8	26.7	-5.7
2a-30-30-VL5-INC5-B	4.5	291	56.9	6.5	-3.5	21.7	-11.5
2a-30-30-VL5-INC5-C	4.9	290	56.5	8.1	-1.9	27.2	-6.3
2a-30-90-VL0-INC5-B	5.2	408	57.2	7.5	-2.3	25.5	-7.5
2a-30-90-VL5-INC5-C	5.5	595	56.5	7.7	-2.4	25.3	-8.1
2a-30-120-VL0-INC5-B	5.2	545	60.7	6.5	-2.4	22.5	-7.9
2a-30-120-VL5-INC5-B	6.0	173	45.5	8.8	-3.6	30.7	-11.4
30-VL5-INC5-B (Single flaw)	6.2	367	54.4	5.6	-5.0	18.6	-16.4
30-VL5-INC5-C (Single flaw)	5.3	504	55.7	8.2	-2.1	27.1	-7.0

The focal mechanisms show that the events are primarily composed of double couple at around 55-60% cumulatively for all tests, followed by isotropic with a proportion of 30%. In all tests, explosion/tensile cracking was more dominant than implosion/anti-cracking, which makes sense given that the hydraulic fracture mechanism is associated with a tensile failure mode (Goncalves and Einstein, 2014). The proportion of DC appears to be relatively consistent amongst tests, with the exception of test 2a-30-120-VL5-B, which appears anomalous in that very few events were detected. Conversely, the proportion of +ISO and –ISO appears to be more variable, even between repeats of the same setup, as seen with the 2a-30-30-VL5 and single flaw results. This may suggest that the amount of volumetric expansion/compression is more closely tied to the specific microstructure around the crack path, where cracks that pass through grains may behave differently from cracks that propagate around grains (Morgan et al, 2013).

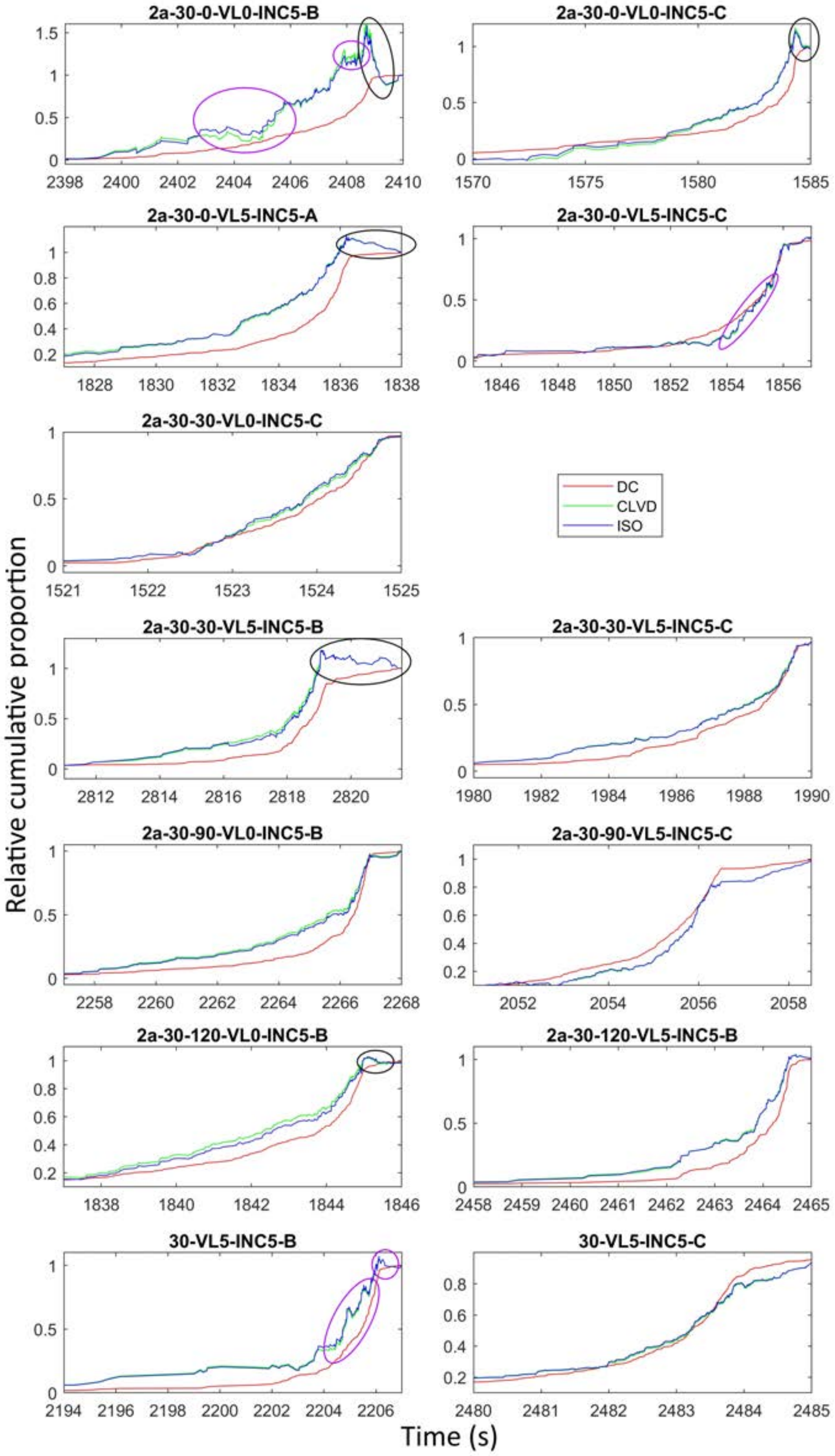

Figure 10: Relative cumulative proportion of DC (red), CLVD (green) and ISO (red) during the last seconds of each test. Black circles indicate significant numbers of implosive NDC events during and after crack propagation, and purple circles indicate periods of cyclic explosive and implosive NDC events. Crack initiation occurs approximately where the curves flatten out towards the end of the experiment.

The time behaviour of the focal mechanisms is presented in Figure 10, which shows that in some tests a significant number of –ISO and –CLVD events occur during and immediately after crack initiation and propagation (highlighted with black circles in the Figure 10). These generally corresponded to tests with higher overall proportions of –ISO and –CLVD as seen in Table 1. However, there does not appear to be any obvious behaviour that could be used as a pre-cursor to this type of behaviour. For example, Figure 10 shows that this can occur in specimens tested at both 0 and 5 MPa of vertical stress, and may only occur in one out of two repeats of the same setup. This again suggests that it is related to the specific microstructure around the crack path. Considering the focal mechanism behaviour prior to crack initiation, we can see that in experiments 2a-30-0-VL0-B, 2a-30-0-VL5-C and 30-VL5-B there appears to be a cyclic behaviour in the cumulative proportion of CLVD and ISO (blue highlights in the figure), where a period of contraction follows one of expansion, indicating microcracks periodically open and close prior to crack initiation. This is analogous to behaviour before earthquakes, as reported by Gao and Crampin (2004), where they show that local compressive stresses near faults decrease before an imminent earthquake.

3.4 Hypocenter Location Analysis

The hypocenter locations are shown in Figure 11. In general, it appears that the hypocenters relate well to the crack path, where the hypocenters are spread over a width of 2-5 mm. It is also noted that the hypocenters in the higher bridging angle geometries (Figures 11h to 11k) are generally more scattered and difficult to interpret than for the lower bridging angle geometries. This may be caused by inaccuracies introduced by the analysis that may be attributed to the overlapping flaws, as the ray paths must travel around the flaws. Overlapping flaws may also generate a more complex stress field leading to a more complex velocity field that is difficult to capture with only eight sensors for velocity measurements. These factors can decrease the accuracy of the localisation procedure. Another factor may be that with the higher bridging angles the more complex stress field generates more possible points of failure, leading to more scattered hypocenters appearing outside of the cracks.

We can make several qualitative observations based on the hypocenter data:

1) The highest concentration of hypocenters tend to be at the flaw tips, where the stress concentration is highest before crack initiation (see also Goncalves da Silva and Einstein, 2014).
2) Significant clustering can also be seen in the coalescence zone of some tests (Figures 11a, 11e and 11i), where a crack forms directly between the inner flaw tips (known as direct coalescence).
3) Tests where cracks emanate from each inner flaw tip and do not connect (Figures 11f and 11g) show few events in the zone directly between the flaws, which is expected given that no crack forms there. However, we note that cracks initiating from the inner flaw tips are associated with fewer hypocenters than those initiating from the outside flaw tips.
4) More events are seen in the coalescence zone of the test shown in Figure 11i than the tests in Figures 11h, 11j and 11k, even though direct coalescence is observed in all four cases. This may be explained when considering the specific crack paths: coalescence in Figure 11i occurs between the middle of the flaws, whereas the other three tests generally show coalescence between the flaw tips. This may be because less energy is required to initiate a crack from a flaw tip since the stress concentration is higher.

5) Many of the tests (Figures 11a, 11b, 11c and 11e) exhibit linear clusters of hypocenters even where no white patching nor cracking occurs. These appear to be more common for lower flaw angles, and are clustered perpendicularly to the flaw orientation.
6) The crack and hypocenter patterns for the single flaw geometries (Figures 11l and 11m) tend to be simpler than the double flaw geometries. It can be seen that in both cases the hypocenter locations migrate away from the flaw tips in time, and that the hypocenters most distant from the flaw tended to be NDC type focal mechanisms. Near the flaw tips, the focal mechanisms tended to be a combination of DC and NDC.
7) The focal mechanisms appear to cluster spatially by type of mechanism. For example in the test shown in Figure 11c, the area around the left outer flaw tip consists primarily of DC dominated events. Analogously, the test shown in Figure 11g produced events at the outer left flaw tip consisting of a mix of focal mechanism, but the area below the flaw tip consists mainly of explosive NDC events. It also appears that events further from the flaws i.e. the most scattered tend to be DC dominated.

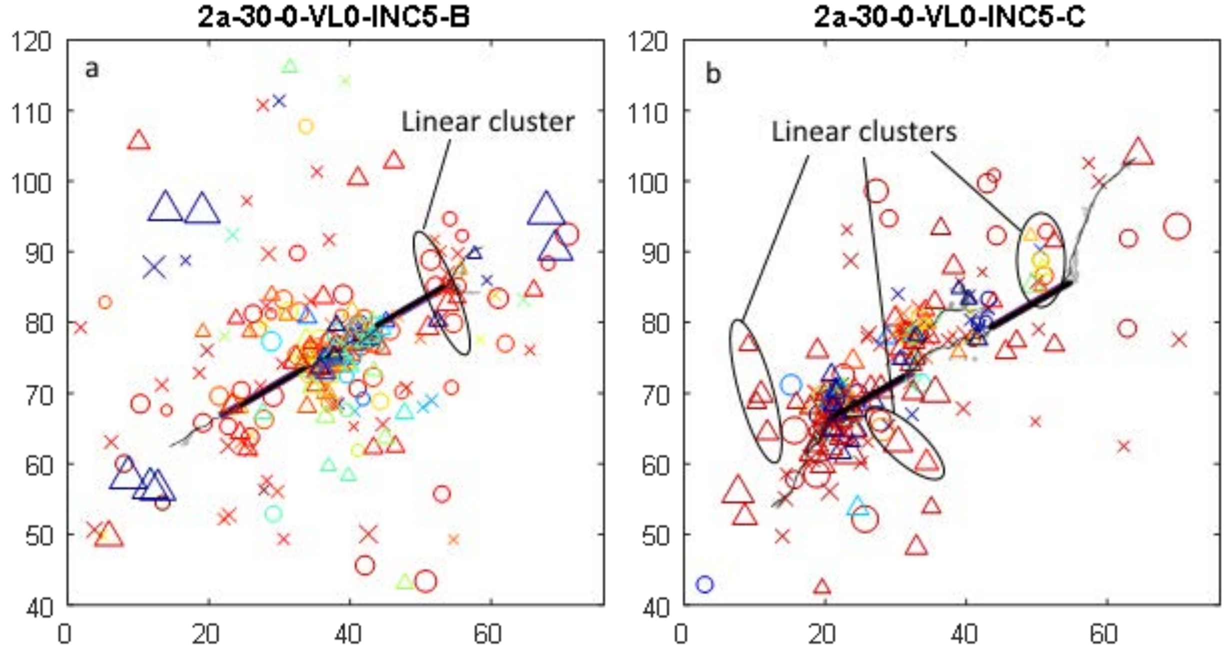

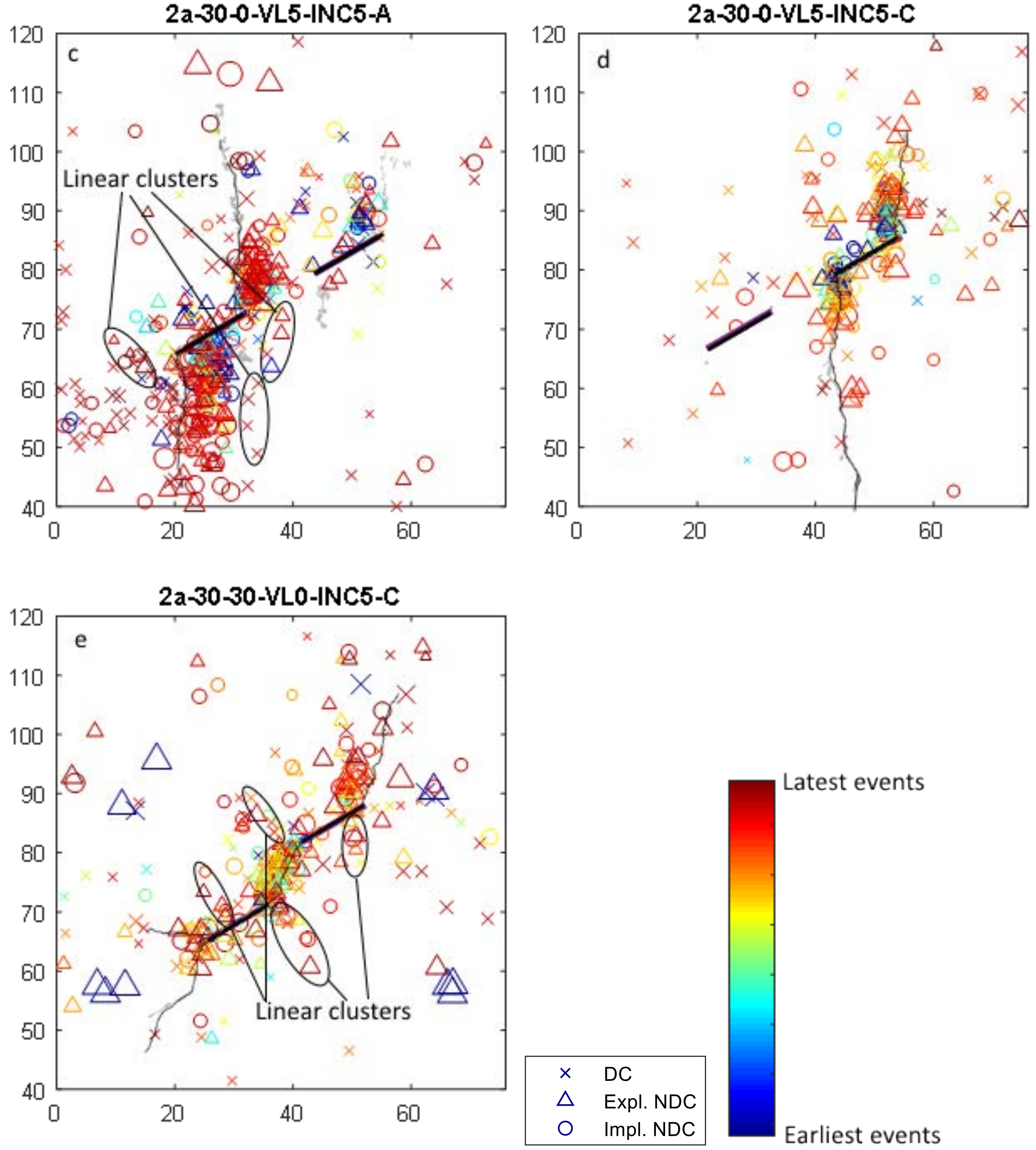
2a-30-0-VL5-INC5-A
c
Linear clusters
2a-30-0-VL5-INC5-C
d
2a-30-30-VL0-INC5-C
e
Linear clusters
120
110
100
90
80
70
60
50
40
0
20
40
60
DC
Expl. NDC
Impl. NDC
Latest events
Earliest events

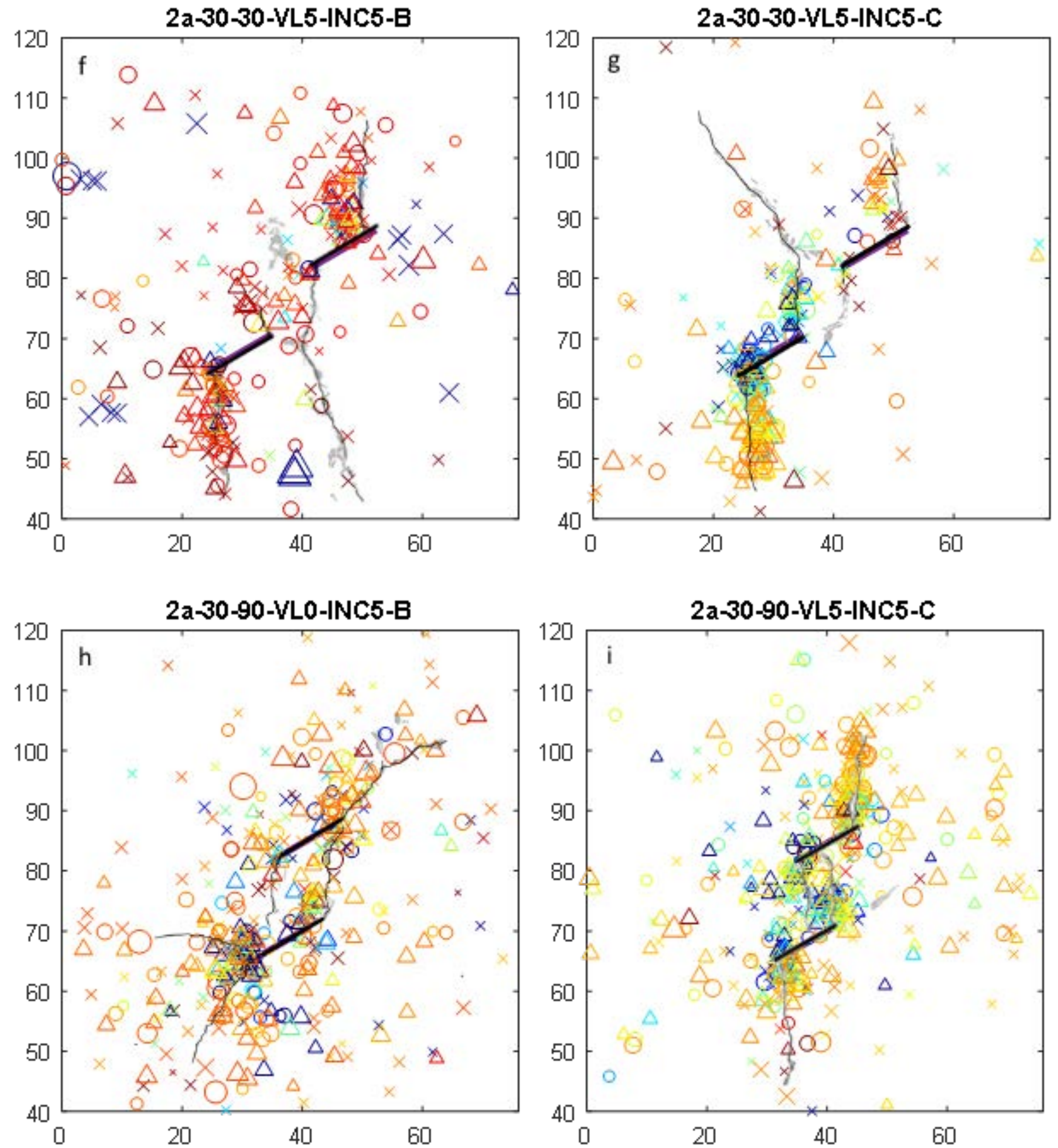
2a-30-30-VL5-INC5-B
f
2a-30-30-VL5-INC5-C
g
2a-30-90-VL0-INC5-B
h
2a-30-90-VL5-INC5-C
i
120
110
100
90
80
70
60
50
40
0
20
40
60

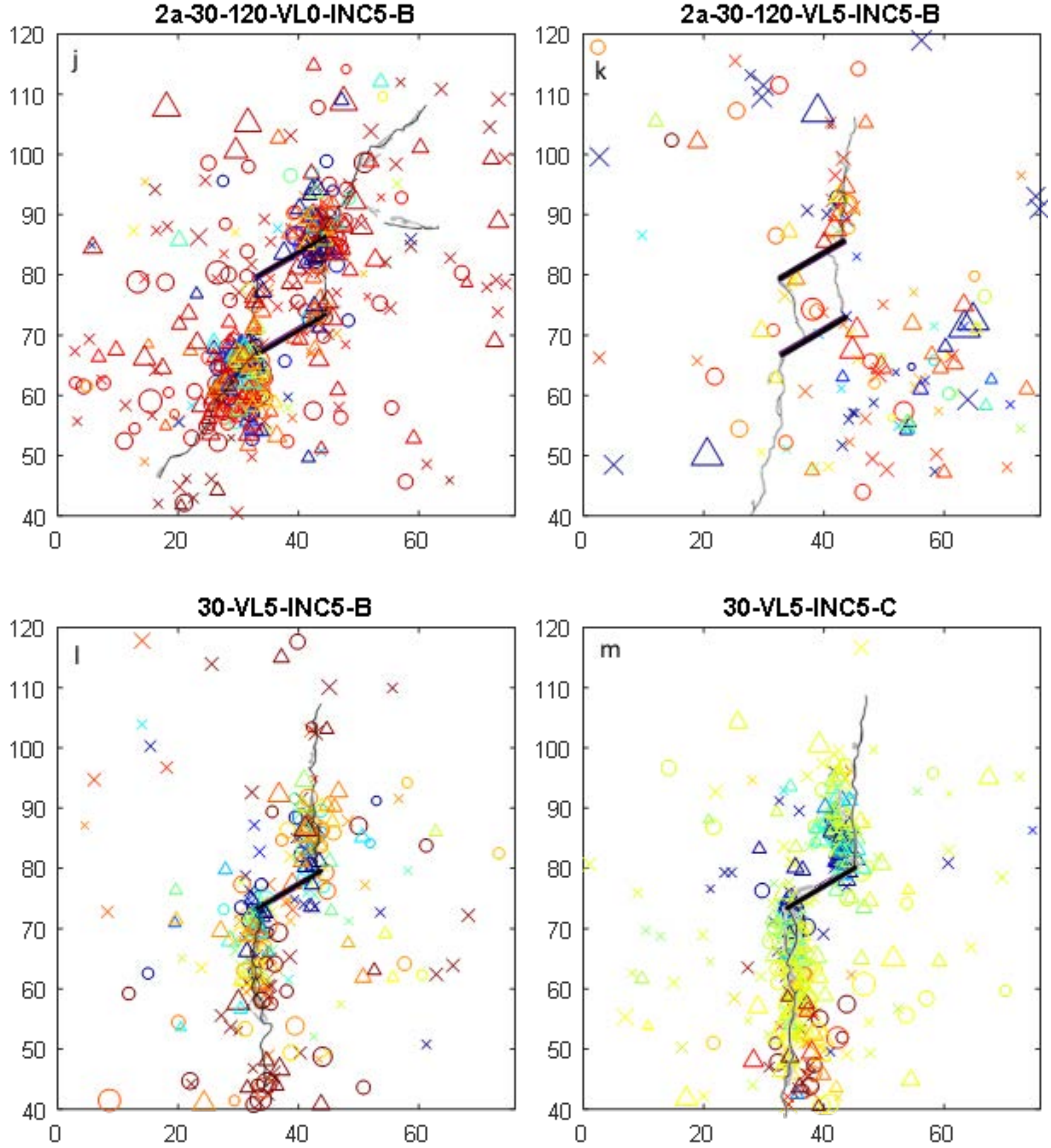
2a-30-120-VL0-INC5-B

2a-30-120-VL5-INC5-B

30-VL5-INC5-B

30-VL5-INC5-C

Figure 11: Hypocenter locations for each test. The magnitude of the event is shown by the size of the data point. Dark grey lines indicate the cracks, and light grey areas indicate white-patching. The symbols indicate whether the event can be classified as double couple (x), explosive non double couple (Δ), or implosive non double couple (o), and colour represents time, where red is the latest event and blue the earliest.

3.5 Spatio-temporal Analysis

This section presents the spatial-temporal development of AE hypocenters for tests 30-VL5-C, 2a-30-0-VL0-C, and 2a-30-120-VL0-B. The hypocenter distributions for these tests are shown in Figure 11. For spatio-temporal analysis, the AE events were ordered sequentially, and divided into six time segments each with equal number of AE events to qualitatively analyse their behaviour. Given that the event rate increases towards the end of the test, this means that the first segment may cover over 100s of the test, while the third frame may cover less than one second. These AE observations are also compared to the visually observed crack development. These three tests are chosen as they most clearly illustrate key findings from all the 13 tests.

3.5.1 30-VL5-INC5-C

We first present the analysis from a test with a single flaw (Figure 12), as this presents a simpler geometry and stress field, resulting in simpler crack patterns and straight ray paths for the AE signals. In this test, we observed a classic wing crack pattern, where crack A initiated from the left tip, then crack B from the right tip. Pressure increases until 2450s and fluctuates until 2484s, at which point the water pressure drops due to crack propagation.

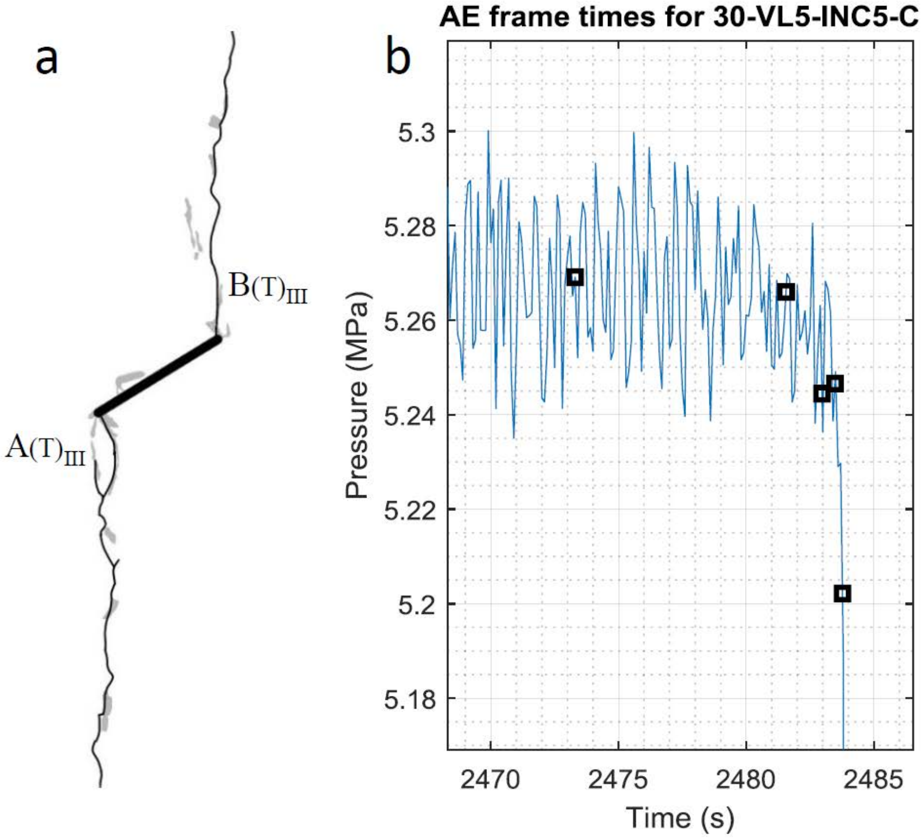

Figure 12: Test 30-VL5-INC5-C (a) Crack sequence shown in alphabetical order. (T) denotes the cracks open in tension, and subscripts refer to crack type as defined in Wong and Einstein (2009). Black lines denote cracks and grey areas indicate white patching. (b) Pressure-time plot for the experiment. Black squares indicate times used in Figure 13.

As seen in figure 13, before 2473 s more AE hypocenters occur at the right tip than the left, and consist of a combination of all focal mechanisms. However, we note that the highest amplitude events at the right flaw tip are explosive NDC type, while the largest events at the left tip consists of implosion and shear. This indicates that the rock at the right tip is opening, which generates a compressive stress field at the left flaw tip. Visually at this time we only see small (2-3 mm) areas of white patching at each flaw tip.

Between 2473 s and 2481 s, at the left flaw tip we continue to see small shear events at the very tip, and primarily implosive events further from the flaw tip. On the right flaw tip we see that a large number of high amplitude explosive events are generated, with the highest amplitudes occurring in a zone approximately 5 mm above the flaw tip. This suggests that the microcracks from the previous frame may have coalesced through a series of tensile microcracks, which follows the general micromechanical model (Brace and Bombolakis, 1963; Nemat-Nasser and Horii, 1982; Ashby and Hallam, 1986; Hoek, 1969) that a crack first forms at existing planes of weakness such as grain boundaries (Morgan et al, 2013). Then if the shear stress exceeds the frictional resistance this can result in the formation of wing cracks that coalesce between the existing shear microcracks. We suggest that this sudden shift in behaviour from implosive NDC and DC dominated events to a number of high amplitude explosive NDC events indicates a coalescence of microcracks similar in nature to those described in Irwin (1958) and Wong and Einstein (2009b). This phenomenon has been observed directly in limited cases in specimens used in the present study, through SEM imaging of areas exhibiting white patching. Figure 14 shows an example, where we see a series of connected en-echelon microcracks connecting into a larger crack feature emanating from a flaw tip.

Between 2481s to 2482.7s we see that there are fewer events than before at the right tip, and that the large ones are associated with mostly explosive and a few implosive NDC events. On the left tip, a linear series of small amplitude explosive events occur near the flaw tip, and larger explosive NDC events occur further from the flaw tip. Visually, the white patching has extended approximately 10 mm from each flaw tip.

Between 2482.7s and 2483.3s the AE hypocenters move outwards from the flaw tips, indicating that the area immediately at the flaw tips is sufficiently damaged that the “microcrack front” has moved outwards from the flaw tips. More large implosive NDC events occur at the right flaw tip, while at the left flaw the events are primarily high amplitude explosive NDC events, indicating that microcrack coalescence occurs at the left tip at this time.

Between 2483.3s and 2483.7s, many high amplitude events occur below the left and above the right flaw tips, and consist of a mix of focal mechanisms. This occurs approximately the same time as macro-crack initiation and propagation.

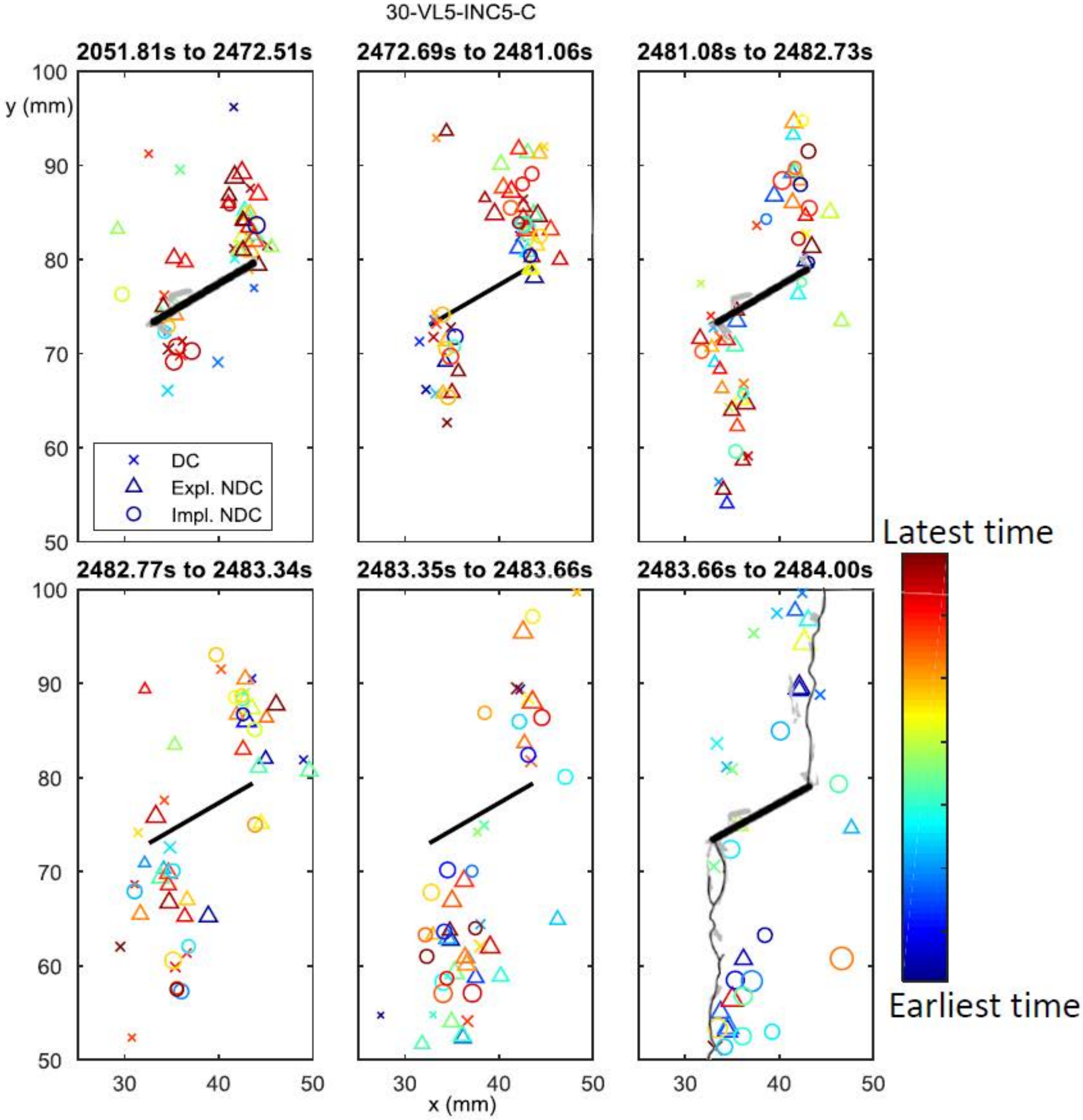

Figure 13: Temporal evolution of AE hypocenters for test 30-VL5-INC5-C. DC events refer to those with higher double couple, or shear content, explosive NDC (non double-couple) to those with lower DC and positive ISO and CLVD components, and implosive NDC to those with lower DC and negative ISO and CLVD. Colour is used to show time, and size indicates magnitude. Visual observations of the white patching (in grey) and cracking extent (in black) are overlaid where applicable.

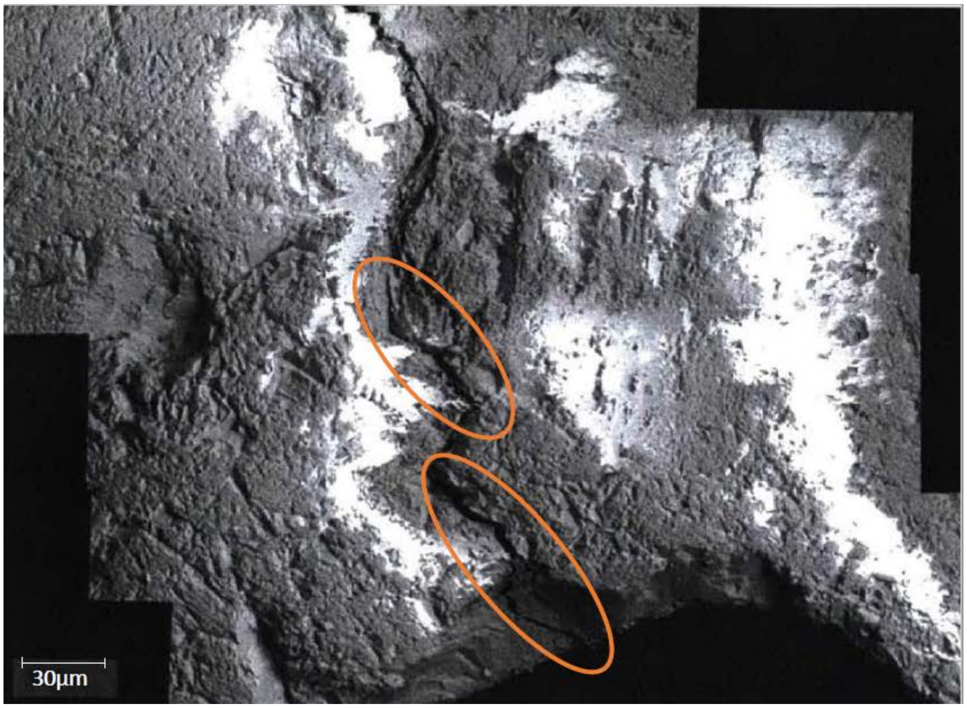

Figure 14: SEM image taken near the flaw tip of test 2a-30-0-VL5-A showing a series of connected en-echelon microcracks, such as the one highlighted in the orange circles. From Goncalves da Silva (2016).

3.5.2 2a-30-0-VL0-C

As seen in Figure 15, tensile crack A initiates first from the outer left flaw tip, followed by tensile crack B which does not coalesce (i.e. propagate to the inner right flaw tip) followed by tensile crack C, which then coalesces with the right flaw after the initiation of tensile crack D. Peak pressure occurs around 1569s, and a local minimum in pressure occurs around 1580s, a few seconds before pressure breakdown as seen in Figure 15.

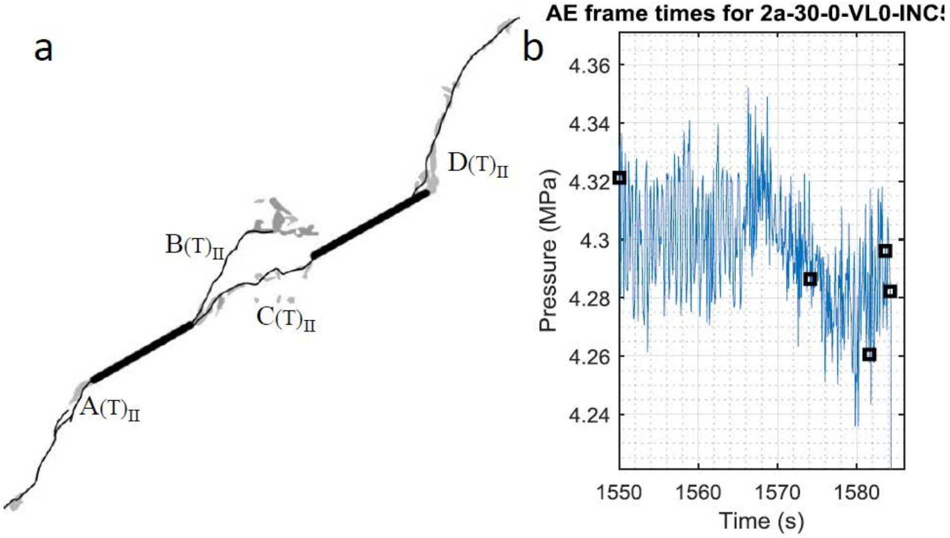

Figure 15: (a) Crack sequence shown in alphabetical order. (T) denotes the cracks open in tension, and subscripts refer to crack type as defined in Wong and Einstein (2009). Black lines denote cracks and grey areas indicate white patching. (b) Pressure-time plot for the experiment. Black squares indicate times used in Figure 16.

In Figure 16, we can see that initially the majority of the high amplitude events are located immediately at the outer left flaw tip, and consist primarily of explosive NDC events. Fewer small amplitude events occur at both inner flaw tips, and consist of a mix of focal mechanisms. Visually, there appears to be 2-3 mm of white patching at all flaw tips.

Between 1554s and 1574s, the largest concentration of events continues at the outer left flaw tip, with predominantly explosive NDC and some DC and implosive NDC events. A small number of high amplitude events also occurs at the inner left flaw tip, and consist primarily of DC and implosive NDC events, implying that opening occurs at the outer left flaw tip, generating a compressive field at the inner left tip.

Between 1574s and 1582s a large number of DC and implosive NDC events occur at both tips of the left flaw, indicating continued microcracking along grain boundaries.

Between 1582 and 1583.6s, a number of large explosive NDC events occur at the inner left flaw tip, while a combination of all focal mechanisms occur at the outer left flaw tip. This indicates microcrack coalescence occurs first at the inner left flaw tip. Visually, the white patching extends by another 2-3 mm.

Between 1583.6s and 1584.2s the events at the outer left tip are mostly explosive NDC, indicating that microcrack coalescence has occurred. At the inner left tip, there are a number of large DC dominated events, which likely corresponds to the formation of crack B.

In the last frame the macro-crack initiates and propagates, and is accompanied by a wide spatial scatter with a combination of focal mechanisms.

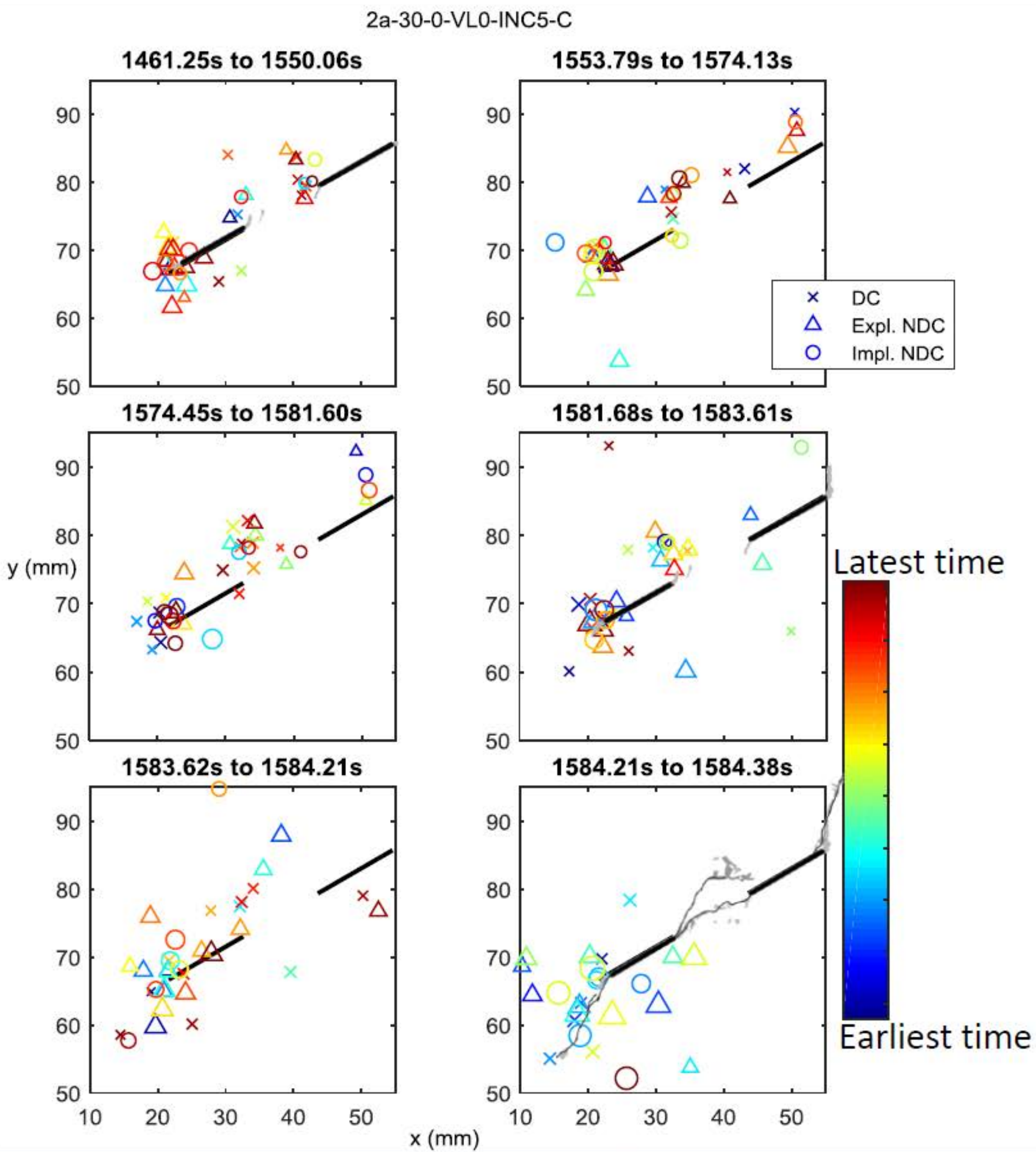

Figure 16: Temporal evolution of AE hypocenters. DC events refer to those with higher double couple, or shear content, explosive NDC (non double-couple) to those with lower DC and positive ISO and CLVD components, and implosive NDC to those with lower DC and negative ISO and CLVD. Colour is used to show time, and size indicates magnitude. Visual observations of the white patching (in grey) and cracking extent (in black) are overlaid where applicable.

3.5.3 2a-30-120-VL0-B

As shown in Figure 17, tensile crack A initiates from the bottom left flaw tip, then tensile crack B from the top right flaw tip. Tensile crack C then initiates from the top left flaw tip, but does not coalesce while tensile crack D initiates from the bottom right flaw tip and coalesces to the top right flaw tip. Water pressure fluctuates between 1800s and 1840s, at which point the water pressure begins to drop.

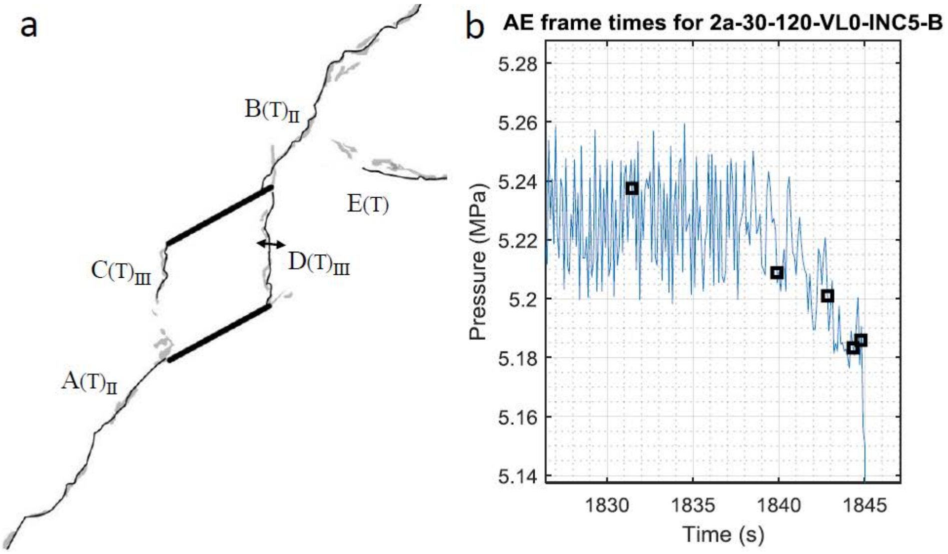

Figure 17: (a) Crack sequence shown in alphabetical order. (T) denotes the cracks open in tension, and subscripts refer to crack type as defined in Wong and Einstein (2009). Black lines denote cracks and grey areas indicate white patching. (b) Pressure-time plot for the experiment. Black squares indicate times used in Figure 18.

Figure 18 shows that up to 1831s the majority of high amplitude events occur around the top right flaw tip, and consist of mostly explosive NDC events with some implosive NDC events. A number of smaller DC events occur closer to the top right flaw tip. At the bottom left flaw tip there is a large number of smaller amplitude events with a mix of focal mechanisms, the highest amplitude of which belong to two explosive and three implosive NDC events. This implies that in this time frame the area above the top right flaw tip is opening, and correspondingly the area below the bottom left flaw tip is under compression as a result of the rigid body movement. A single large explosive NDC event also occurs at each of the tips of the top left and bottom right flaws, which are the initiation points for cracks C and D. Visually, there is 2-3mm of white patching on the top left and bottom right flaw tips, and longer 4-5mm white patching at the top right flaw tip. This corresponds to the AE focal mechanism suggesting primarily opening at the top right.

From 1831.5 to 1840s, the majority of AE events occur at the left tip of the bottom flaw, where the largest amplitude events occurs very close to the flaw tip as explosive NDC type. A general cloud of smaller primarily DC events surrounds the NDC events.

Between 1840s and 1842.8s large explosive NDC continue to occur around the bottom left flaw tip, but the general cloud of hypocenters moves away from the flaw tip as the zone of intense damage moves downwards. A clear linear cluster of large explosive NDC events also occurs along the path of crack D, indicating that microcracks have created the white patching along crack D seen visually in the next frame.

Between 1842.9s and 1844.3s we note an interesting phenomenon at both the top right and bottom left flaw tips where there is a zone of explosive NDC events adjacent to a zone of implosive NDC events, likely related to compressive stresses at grain boundaries as a result of microcrack opening nearby. This is further discussed in section 3.6. We also see large amplitude explosive NDC events at all the flaw tips. This corresponds well to the visual observation that white patching has developed to 4-5 mm at all flaw tips.

Between 1844.3s and 1844.76s the events near the flaw tips are primarily implosive NDC, while explosive NDC events occur further away from the flaw tips. In the last frame (1844.76s to 1845.09s) we can see that the crack has propagated, and that the accompanying AE events are primarily explosive NDC and appear to be closely aligned with the crack path.

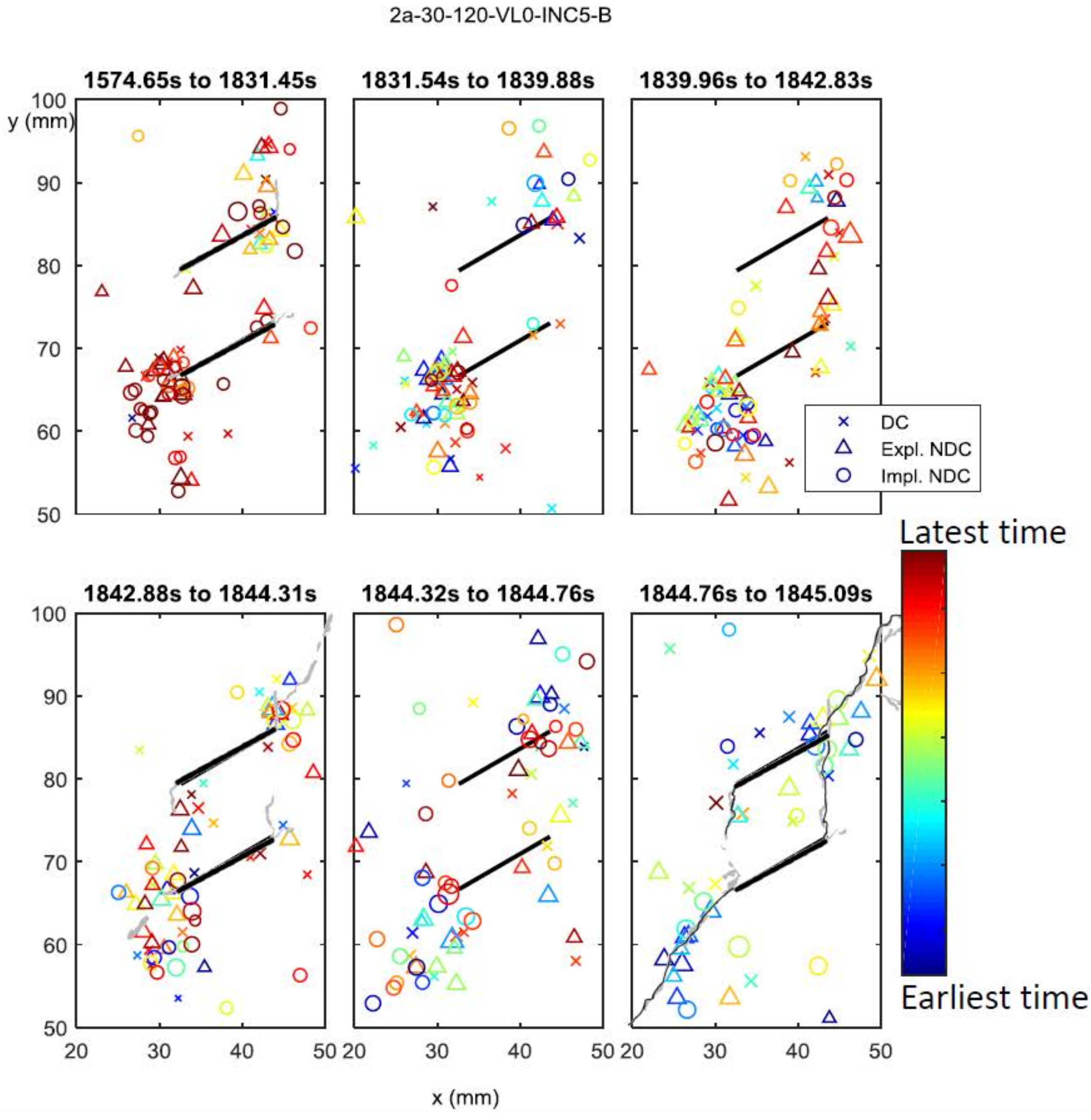

Figure 18: Temporal evolution of AE hypocenters. DC events refer to those with higher double couple, or shear content, explosive NDC (non double-couple) to those with lower DC and positive ISO and CLVD components, and implosive NDC to those with lower DC and negative ISO and CLVD. Colour is used to show time, and size indicates magnitude. Visual observations of the white patching (in grey) and cracking extent (in black) are overlaid where applicable.

3.6 Discussion

In many tests, we observe a phenomenon where explosive NDC are spatially distinct from implosive NDC events. This can be seen at two scales: firstly at opposite ends of a flaw, where opening at one flaw tip generates a compressive stress field at the other flaw tip. Secondly, we see locally (~few mm) separated zones of explosive/implosive NDC events in test 30-VL5-C (Figure 13)between 2483.35 and 2483.66 below the left flaw tip and in test 2a-30-120-VL0-B (Figure 18) between 1842.9s and 1844.3s at the top right and bottom left flaw tips. This may be caused by microcracks opening through a grain, resulting in compression of an adjacent grain boundary. This is shown in Figure 19, which is a photo of the bottom left flaw tip and the area below it, overlain with AE events that occurred throughout the experiment. We can see that in general the AE events tended to occur along grain boundaries.

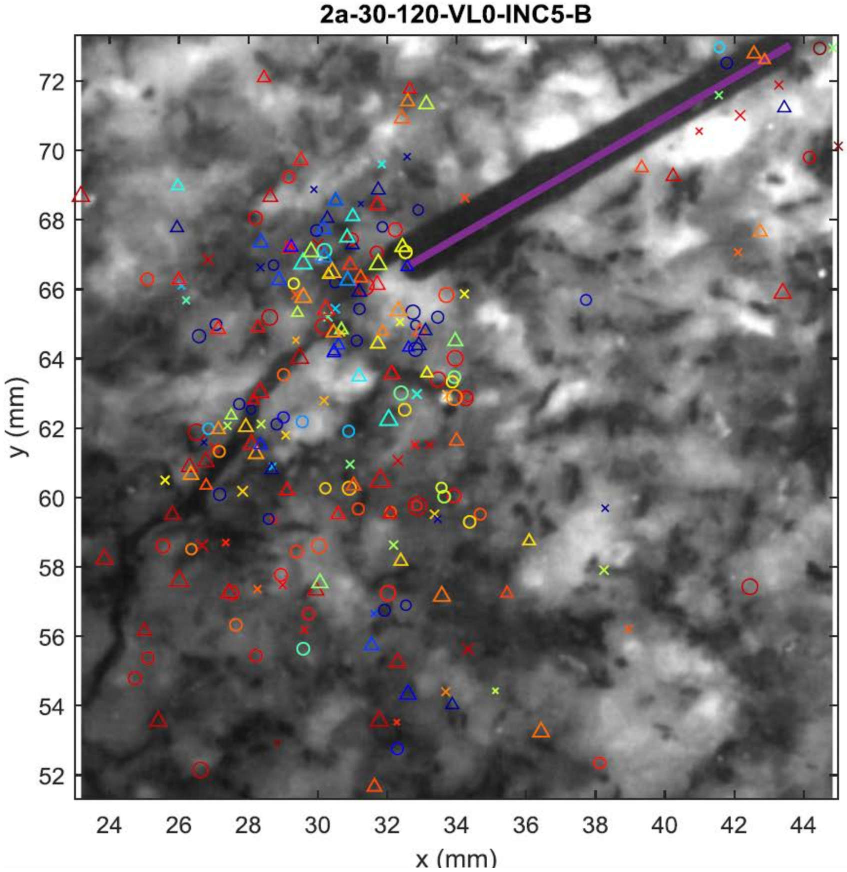

Figure 19: Zoomed photo of the bottom flaw of test 2a-30-120-VL0-B and the area below and to the left of it, overlain by AE events occurring throughout the test. Colour refers to time where red is the latest, crosses refer to DC dominated events, triangles to explosive NDC events and circles to implosive NDC events. The size of the symbols represents the magnitude of the events.

At this point it is also possible to evaluate in general the relation between AE and visual observations. This is shown in Table 2, where we describe the similarity of the spatial distribution observed with the two methods, and assess the possibility of using AE as a predictor of the crack initiation point.

Table 2: Summary table showing a) where there are AE hypocenters, whether these coincide with visually identified damage, b) where there is visually identified damage, whether AE hypocenters occur there , c) whether the point of crack initiation (first crack to form) corresponds to a high concentration of AE hypocenters, d) whether there were multiple clusters of hypocenters i.e. whether one could have made a unique prediction on the point of crack initiation.

Co-planar	Are most cracks/white patching reflected by AE?	Do most AE hypocenters coincide with cracking/white patching?	Could the AE predict crack initiation?	Can one make a single prediction?
2a-30-0-VL0-B	N	N	Y	N
2a-30-0-VL0-C	N	Y	Y	Y
2a-30-0-VL5-A	N	Y	Y	Y
2a-30-0-VL5-C	Y	Y	Y	N
Flat bridging angle				
2a-30-30-VL0-C	N	Y	N	N
2a-30-30-VL5-B	Y	N	Y	N
2a-30-30-VL5-C	Y	Y	Y	Y
Steep bridging angle				
2a-30-90-VL0-B	N	Y	Y	Y
2a-30-90-VL5-C	N	Y	Y	N
2a-30-120-VL0-B	N	N	Y	N
2a-30-120-VL5-B	N	Y	?	Y
Single Flaw				
30-VL5-B	Y	Y	Y	N
30-VL5-C	Y	Y	Y	N

Overall we can see that the visual crack and white patching tended to be a subset of the AE hypocenter coverage. Of the AE hypocenters that were not associated with visually identified microcracking, we assume that many were associated with areas of damage we could not visually ascertain, such as the anti-wing cracks discussed in Section 3.4. Nevertheless, we determine that in most cases, the flaw tip from which the crack initiates corresponds to an area with a high concentration of AE hypocenters, such that one could predict it as an initiation point. However, we also note that, in general, the data often showed two or three flaw tips with significant hypocenter coverage, indicating that one would not be able to make a single prediction given AE data, but nevertheless narrow the possibilities to a few locations of crack initiation.

4 Summary and Conclusions

We presented the acquisition, analysis and interpretation of acoustic emissions data from a series of laboratory hydraulic fracture experiments on granite. These data are related to corresponding visual observations made using high resolution and high speed imaging. The main results are summarised as follows:

- The rate of AE hits tends to be close to zero until 80% of the peak water pressure, at which point it increases exponentially. In some experiments; it was observed that there was a second inflection where the rate of AE accelerated, close to the time of failure.
- Analysis of the focal mechanisms revealed that, overall, approximately 55-60% of the radiation pattern could be explained by a double couple mechanism, while approximately 25-30% represent isotropic contributions. Explosive non-double-couple events tended to be more common than implosive non-double-couple events until the end of the test, at which point a significant number of implosive events occur in some tests
- Hypocenter locations of AE events generally correspond well to the cracks and white patching (zones of microcracks or process zone), with the highest concentration of hypocenters occurring at the flaw tips. In particular, the single flaw geometries showed the spatial growth of hypocenters away from the flaw tips over time
- Spatio-temporal analysis of the visual and AE data revealed behaviour where, initially, the focal mechanisms consisted of mixed focal mechanism events until a point in time where many high amplitude explosive non-double-couple events occur over a short period of time. We suggest that the latter represents coalescence of microcracks and is a key pre-cursor to hydraulically induced cracking.
- Based on spatio-temporal analyses of all tests, we suggest that the visually observed microcracking tends to be related to damage, and that the AE, in general, could predict the point of crack initiation. However, this prediction may not be unique given that there are often two to three concentrations of AE hypocenters.

We can therefore conclude that under stress conditions where the failure is driven by fluid pressure with multiple points of crack initiation, the observed acoustic emissions present a reasonably complete picture of the areas of microcracks, and have a good potential to be used to predict the final crack pattern and the points of crack initiation.

Acknowledgements

The research presented in this paper was supported by TOTAL SA. The authors would like to express their sincere gratitude for this support. We would also like to thank Professors John Germaine and German Prieto for the insights and suggestions.

References

Ashby, M. and Hallam, S. (1986). The failure of brittle solids containing small cracks under compressive stress states. Acta Metallurgica, pages 497-510.

Brace, W. and Bombolakis, E. (1963). A note on brittle crack growth in compression. Journal of Geophysical Research, pages 3709-3713.

Bredehoeft, J., Wol, R., Keys, W., and Shuter, E. (1976). Hydraulic fracturing to determine the regional stress field, Piceance basin, Colorado. Geological Society of America Bulletin, 87:250-258.

Bunger, A., Kear, J., Dyskin, A., and Pasternak, E. (2004). Interpreting post- injection acoustic emission in laboratory hydraulic fracturing experiments. In 48th US Rock Mechanics/Geomechanics Symposium.

Dresen, G., Stanchits, S., and Rybacki, E. (2010). Borehole breakout evolution through acoustic emission location analysis. International Journal of Rock Mechanics and Mining Sciences, pages 426-435.

Douillet-Grelliera, T., Jones, B.D.,Pramanik, R., Pan, K Albaiz, A., Williams, J.R. (2016) Mixed-mode fracture modeling with smoothed particle hydrodynamics. Computers and Geotechnics. 79:73-85

Frash, L. (2014). Laboratory-scale study of hydraulic fracturing in heterogeneous media for enhanced geothermal systems and general well stimulation. PhD thesis, Colorado School of Mines.

Gao, Y. and Crampin S. (2004) Observations of stress relaxation before earthquakes. Geophysical Journal International. 157:2:578-582

Goncalves da Silva, B. and Einstein, H. (2018). Physical processes involved in the laboratory hydraulic fracturing of granite: Visual observations and interpretation. 191:125-142

Goncalves da Silva, B. M. (2016). Fracturing processes and induced seismicity due to the hydraulic fracturing of rocks. PhD thesis, Massachusetts Institute of Technology.

Goncalves da Silva, B. and Einstein, H. H. (2014). Finite element study of fracture initiation in flaws subject to internal fluid pressure and vertical stress. International Journal of Solids and Structures, pages 177-204.

Goncalves da Silva, B., Li, B. Q., Moradian, Z., Germaine, J., and Einstein, H. H. (2015). Development of a test setup capable of producing hydraulic fracturing in the laboratory with image and acoustic emission monitoring. In 49th U.S. Rock Mechanics/Geomechanics Symposium.

Graham, C., Stanchits, S., Main, I. G., and Dresen, G. (2010). Comparison of polarity and moment tensor inversion methods for source analysis of acoustic emission data. International Journal of Rock Mechanics and Mining Sciences, pages 161-169.

Hoek, E. (1969). Rock Mechanics in Engineering Practice, chapter Brittle Failure of Rock. John Wiley and Sons

Irwin, G. (1958). Elasticity and Plasticity, chapter Fracture. Springer.

Ishida, T. (2001). Acoustic emission monitoring of hydraulic fracturing in laboratory and field. Construction and Building Materials, pages 283-295.

Julian, B. and Sipkin, S.A. (1985). Earthquake processes in the Long Valley Caldera Area, California. Journal of Geophysics Research: Solid Earth. 90:11155-11169

Li, B. Q. and Einstein, H. (2017). Comparison of visual and acoustic emission observations in a four point bending experiment on barre granite. Rock Mechanics and Rock Engineering, 2277-2296.

Li, B. Q., Moradian, Z., Goncalves da Silva, B., and Germaine, J. (2015). Observations of acoustic emissions in a hydraulically loaded granite specimen. In 49th U.S. Rock Mechanics/Geomechanics Symposium.

Liu, Q., Xu, X., Tsutomo, Y., and Akio, C. (2001). Mechanical properties of tgp granite in dependence on temperature and time. In ISRM International Symposium- 2nd Asian Rock Mechanics Symposium, Beijing, China.

Maeda, N. (1985). A method for reading and checking phase times in autoprocessing system of seismic wave data. Journal of the Seismological Society of Japan, 38:365-379.

Matsunaga, I., Kobayashi, H., Sasaki, S., and Ishida, T. (1993). Studying hydraulic fracturing mechanism by laboratory experiments with acoustic emission monitoring. International Journal of Rock Mechanics and Mining Sciences and Geomechanics Abstracts, 30(7):909-912.

Mayr, S., Stanchits, S., Langenbruch, C., Dresen, G., and Shapiro, S. (2011). Acoustic emission induced by pore-pressure changes in sandstone samples. Geophysics, 76:MA21-MA32.

McLaskey, G. C., Lockner, D. A., Kilgore, B. D., and Beeler, N. M. (2015). A robust calibration technique for acoustic emission systems based on momentum transfer from a ball drop. Bulletin of the Seismological Society of America, 105:257-271.

Moradian, Z., Ballivy, G., Rivard, P., Gravel, C., and Rousseau, B. (2010). Evaluating damage during shear tests of rock joints using acoustic emissions. International Journal of Rock Mechanics and Mining Sciences, 1:590-598.

Moradian, Z., Einstein, H. H., and Ballivy, G. (2016). Detection of cracking levels in brittle rocks by parametric analysis of the acoustic emission signals. Rock Mechanics and Rock Engineering, 1:785-800.

Morgan, S., Johnson, C., and Einstein, H. (2013). Cracking processes in barre granite: fracture process zones and crack coalescence. International Journal of Fracture, 180:177-204.

Nemat-Nasser, S. and Horii, H. (1982). Compression-induced nonplanar crack extension with application to splitting, exfoliation, and rockburst. Journal of Geophysical Research, pages 6805-6821.

Ohtsu, M. (1995). Acoustic emission theory for moment tensor analysis. Research in Nondestructive Evaluation, 6(3):169-184.

Ohtsu, M. (2000). Moment tensor analysis of ae and sigma code. Acoustic Emission-Beyond the Millennium, pages 19-34.

Savic, M., Cockram, M., and Ziolkowski, A. (1993). Ultrasonic monitoring of hydraulic fracturing experiments. In I55th EAEG Meeting.

Shearer, P. M. (2009). Introduction to Seismology. Cambridge University Press.

Stanchits, S., Fortin, J., Gueguen, Y., and Dresen, G. (2009). Initiation and propagation of compaction bands in dry and wet bentheim sandstone. Rock Physics and Natural Hazards, pages 846-868.

Stanchits, S., Mayr, S., Shapiro, S., and Dresen, G. (2011). Fracturing of porous rock induced by uid injection. Tectonophysics, pages 129-145.

Stoeckhert, F., Molenda, M., Brenne, S., and Alber, M. (2015). Fracture propagation in sandstone and slate - laboratory experiments, acoustic emissions and fracture mechanics. Journal of Rock Mechanics and Geotechnical Engineering, pages 237-249.

Vavryčuk, V. (2015). Moment tensor decomposition revisited. Journal of Seismology. 19:231:252

Wong, L.N.Y. and Einstein, H. (2009). Crack coalescence in molded gypsum and carrara marble: part 1 - macroscopic observations and interpretation. Rock mechanics and Rock Engineering, pages 475–511.

Wong, L.N.Y. and Einstein, H. (2009). Crack Coalescence in Molded Gypsum and Carrara Marble: Part 2—Microscopic Observations and Interpretation. Rock Mechanics and Rock Engineering. Pages 513-545

Yoshimitsu, N., Kawakata, H., and Takahashi, N. (2014). Magnitude -7 level earthquakes: A new lower limitof self-similarity in seismic scaling relationships. Geophysical Research Letters, 41:4495-4502.